

Integration Flow Models

Jingjing Wang^{*1} Dan Zhang^{*1} Joshua Luo¹ Yin Yang² Feng Luo¹

Abstract

Ordinary differential equation (ODE) based generative models have emerged as a powerful approach for producing high-quality samples in many applications. However, the ODE-based methods either suffer the discretization error of numerical solvers of ODE, which restricts the quality of samples when only a few NFEs are used, or struggle with training instability. In this paper, we proposed Integration Flow, which directly learns the integral of ODE-based trajectory paths without solving the ODE functions. Moreover, Integration Flow explicitly incorporates the target state \mathbf{x}_0 as the anchor state in guiding the reverse-time dynamics. We have theoretically proven this can contribute to both stability and accuracy. To the best of our knowledge, Integration Flow is the first model with a unified structure to estimate ODE-based generative models and the first to show the exact straightness of 1-Rectified Flow without reflow. Through theoretical analysis and empirical evaluations, we show that Integration Flows achieve improved performance when it is applied to existing ODE-based models, such as diffusion models, Rectified Flows, and PFGM++. Specifically, Integration Flow achieves one-step generation on CIFAR10 with FIDs of 2.86 for the Variance Exploding (VE) diffusion model, 3.36 for rectified flow without reflow, and 2.91 for PFGM++; and on ImageNet with FIDs of 4.09 for VE diffusion model, 4.35 for rectified flow without reflow and 4.15 for PFGM++.

1. Introduction

Recently, ODE-based generative models have emerged as a cutting-edge method for producing high-quality samples in many applications including image, audio (Kong et al., 2021; Popov et al., 2022), and video generation (Rombach et al., 2022; Saharia et al., 2022; Ho & Salimans, 2022). Generally, these methods typically involve learning continuous transformation trajectories that map a simple initial distribution (i.e. Gaussian noise) to the target data distribution (i.e. images) by solving ODEs (Figure 1).

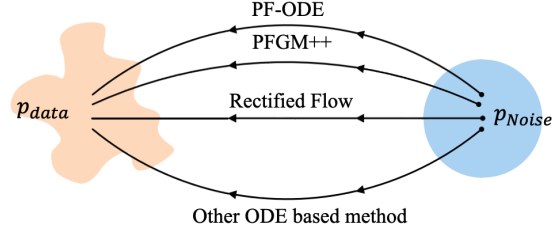


Figure 1. An illustration of ODE-based methods, including PF-ODE, PFGM++, and Rectified Flow.

Among those ODE-based models, the diffusion models have attracted the most attention due to their exceptional ability to generate realistic samples. The diffusion models add noise through a forward diffusion process and gradually remove it in a reverse process that can be reformulated as a probability flow ODE (PF-ODE) (Song et al., 2020b). Despite their success, PF-ODE-based diffusion models face drawbacks due to their iterative nature, leading to high computational costs and prolonged sampling times during inference.

Another ODE-based approach, rectified flow models (Liu et al., 2022; Lipman et al., 2022), focused on learning smoother ODE trajectories to reduce truncation errors during numerical integration. By reducing the curvature of the generative paths, rectified flow enhances sampling efficiency and decreases the computational burden. However, even with smoother trajectories, rectified flow models still require considerable iterations or reflow to produce high-quality samples.

Inspired by concepts from electrostatics, Poisson Flow Generative Models (PFGM) ++ (Xu et al., 2022; 2023), developed the flow-based generative process that solves an ODE derived from the Poisson equation, tracing a path from a simple initial distribution (e.g., noise on a large hemisphere) to the target data distribution residing on a lower dimensional hyperplane. Like the diffusion models and rectified flow, PFGM++ requires multiple steps during inference.

All aforementioned methods required multiple steps of solving different ODE functions in inference to obtain high-quality results. Furthermore, the ODE-based models naturally inherit the discretization error of numerical solvers of ODE, which restricts the quality of samples when only a few

numbers of function evaluations (NFEs) are used or struggle with training instability when neural ODEs are used to approximate the ODE solution using neural networks. Given these challenges associated with ODE-based models, a natural question arises: can we learn the result of ODE-based trajectory paths directly without solving the ODE functions? Therefore, we can take the ODE function-defined generative model and solve this without an ODE solver. The answer is yes. Here we proposed **Integration Flow**, to the best of our knowledge, the first model with the unified structure to estimate ODE-based generative models.

Integration Flows represent a new type of generative model. Unlike traditional ODE-based approaches that focus on approximating the instantaneous drift term of an ODE or depend on iterative sampling methods, Integration Flows directly estimate the integrated effect of the cumulative transformation dynamics over time. This holistic approach allows for the modeling of the entire generative path in a single step, bypassing the accumulation of errors associated with high-curvature trajectories and multiple function evaluations. Integration Flows do not employ the ODE solver and eliminate the need for multiple sampling iterations, significantly reducing computational costs and enhancing efficiency.

Furthermore, to increase the training stability and accuracy in reconstructing, Integration Flow explicitly incorporates the target state \mathbf{x}_0 as the anchor state in guiding the reverse-time dynamics from the intermediate state \mathbf{x}_t . We have theoretically proven that incorporating the target state \mathbf{x}_0 as the anchor state can provide a better or at least equal accurate estimation of \mathbf{x}_0 .

In summary, Integration Flows addresses the limitations of existing ODE-based generative models by providing a unified and efficient approach to model the transformation between distributions. Our contributions can be outlined as follows:

- **Introduction of Integration Flows:** We present Integration Flows, a novel generative modeling framework that estimates the integrated dynamics of continuous-time processes without relying on iterative sampling procedures or traditional ODE solvers, that is, it supports one-step generation for (any) well-defined ODE-based generative models.
- **Unified ODE-Based Generative Modeling:** Integration Flows can adapt different ODE-based generative processes, offering flexibility and unification across different generative modeling approaches.
- **Enhanced Sampling Efficiency and Scalability:** Through empirical evaluations, we show that Integration Flows achieve improved sampling efficiency

and scalability compared to existing ODE-based models, such as diffusion models, Rectified Flows, and PFGM++. In particular, we set the state-of-the-art performance for one-step generation using Rectified Flow and PFGM++.

2. Related Works

Our approach is related to existing works aiming to address the drawbacks of iterative inference in traditional diffusion models (Ho et al., 2020; Song et al., 2020b). Consistency Models (CMs) (Song et al., 2023), for instance, learn a direct mapping from the noisy data distribution to clean samples in a way that is consistent across different noise levels. One major drawback of CM is that it requires enhanced training techniques to achieve good results (Song & Dhariwal, 2023). These improved techniques are specifically tailored to the VE diffusion model, lacking generalizability to other generative models such as Rectified Flow or those employing different noise schedulers like Variance Preserving (VP). This limits the flexibility and extensibility of CMs in broader applications.

Adapting CM to other generative models needs a special redesign of the model. For example, Consistency-FM (Yang et al., 2024) adapted the concept of CM and directly defines straight flows that start from different times to the same endpoint. Consistency-FM improved the quality of samples moderately to the original FM, which is still far below ours. Moreover, 2-Rectified Flow++ (Lee et al., 2024) uses a similar framework of CMs and incorporates different loss and time scheduling and obtain an improved performance on 2-rectified flow. However, reflow needs more computational resources.

Consistency Trajectory Models (CTMs) (Kim et al., 2024) introduce adversarial training to improve sample fidelity. However, adversarial training is notoriously difficult to train, often leading to issues such as mode collapse and training divergence (Sauer et al., 2023). As a result, CTM reduces training stability.

Directly Denoising Diffusion Models (DDDMs) (Zhang et al., 2024), are the most relevant to our work but are limited to the VP case and can be seen as a special case of Integration Flow Models. Unlike DDDMs, our method provides a generalized approach that can be seamlessly extended to various generative models and noise schedulers without the need for model-specific training techniques. Integration Flow offers a more versatile and efficient solution for high-quality sample generation in a single step.

3. Method

In this section, we will introduce the Integration Flow Models based on the general form of ODE-based generative models.

3.1. general form of ODE-based generative models

Consider an initial state \mathbf{x}_T drawn from a distribution $p(\mathbf{x}_T)$, typically chosen to be a simple distribution such as a Gaussian. The goal is to estimate \mathbf{x}_0 , which is aligned with the data distribution p_{data} , by mapping \mathbf{x}_T back through a continuous transformation process. Let $\{\mathbf{x}_s\}_{s=0}^T$ represent a continuous transformation trajectory from \mathbf{x}_T to \mathbf{x}_0 , where \mathbf{x}_s denotes the state at intermediate time $s \in [0, T]$. To describe the reverse-time dynamics that map \mathbf{x}_T back to \mathbf{x}_0 , we define a reverse-time ODE:

$$\frac{d\mathbf{x}_s}{ds} = v(\mathbf{x}_s, s), \quad (1)$$

where $v : \mathbb{R}^n \times [0, T] \rightarrow \mathbb{R}^n$ is a continuous function defining the system's dynamics in reverse time.

The process of obtaining \mathbf{x}_0 from \mathbf{x}_T involves solving this reverse-time ODE, which can be understood as computing the integral:

$$\int_T^0 \frac{d\mathbf{x}_s}{ds} ds = \int_T^0 v(\mathbf{x}_s, s) ds \iff \mathbf{x}_0 = \mathbf{x}_T + \int_T^0 v(\mathbf{x}_s, s) ds \quad (2)$$

The solution of the reverse-time ODE aligns marginally in distribution with the forward process, meaning that the distribution of \mathbf{x}_0 obtained by solving the reverse ODE starting from $\mathbf{x}_T \sim p_T(\mathbf{x})$ approximates the target distribution p_{data} .

While traditional ODE solvers and neural ODE methods are commonly used to solve the (2), they have notable drawbacks. The numerical solvers of ODE can not avoid the discretization error (Bortoli et al., 2023), which restricts the quality of samples when only a few NFEs are used. Second, neural ODEs (Chen et al., 2018), which approximate the ODE solution using neural networks, face a high challenge during gradient backpropagation due to their high memory consumption (Gholami et al., 2019).

3.2. Integration Flows

To overcome the challenges associated with ODE solvers and neural ODEs, we propose Integration Flow to directly estimate the integrated effect of continuous-time dynamics. The cumulative effect of the reverse-time dynamics over the interval $[0, t]$, which is defined in integral $\int_t^0 v(\mathbf{x}_s, s) ds$,

can be obtained as:

$$\int_t^0 v(\mathbf{x}_s, s) ds = V(\mathbf{x}_0, 0) - V(\mathbf{x}_t, t) \quad (3)$$

where $V(\mathbf{x}_s, s)$ is an antiderivative of $v(\mathbf{x}_s, s)$ with respect to s . Then, we defined a function $G(\mathbf{x}_0, \mathbf{x}_t, t)$ as follows:

$$G(\mathbf{x}_0, \mathbf{x}_t, t) := V(\mathbf{x}_t, t) - V(\mathbf{x}_0, 0) \quad (4)$$

This function encapsulates the total influence of the dynamics from an intermediate time t to the final time 0, which leads to the equation:

$$\mathbf{x}_0 = \mathbf{x}_t - G(\mathbf{x}_0, \mathbf{x}_t, t). \quad (5)$$

Next, we define the function:

$$g(\mathbf{x}_0, \mathbf{x}_t, t) := \mathbf{x}_t - G(\mathbf{x}_0, \mathbf{x}_t, t). \quad (6)$$

Therefore, we have:

$$\mathbf{x}_0 = g(\mathbf{x}_0, \mathbf{x}_t, t). \quad (7)$$

Thus, $g(\mathbf{x}_0, \mathbf{x}_t, t)$ is the **solution** of the reversed time ODE from initial time t to final time 0, which encapsulates the cumulative effect of the reverse dynamics from the initial time t to the final time 0, providing an accumulation description of how the target state \mathbf{x}_0 transformed from the intermediate state \mathbf{x}_t .

Integration Flow explicitly incorporates the target state \mathbf{x}_0 as the anchor state in guiding the reverse-time dynamics from the intermediate state \mathbf{x}_t , which contributes to both stability and accuracy in reconstructing \mathbf{x}_0 from intermediate states \mathbf{x}_t . Since Integration Flow bypasses the ODE solver, it provides a unified framework for ODE-based generative models, allowing for one-step generation across a variety of processes.

3.3. Neural Network Approximation

We can implement G using a neural network parameterized by θ (Zhang et al., 2024). The approximated predictive model is thus defined as:

$$g_\theta(\mathbf{x}_0, \mathbf{x}_t, t) = \mathbf{x}_t - G_\theta(\mathbf{x}_0, \mathbf{x}_t, t) \quad (8)$$

where G_θ approximates G .

Equation 8 works well when noise variance is scaled to unit variance, namely Variance Preserving (VP) of diffusion model (Zhang et al., 2024). However, if the noise variance is large, such as the Variance Exploring (VE) cases of diffusion model or the PFGM++ model (shown in section 4), the neural network becomes unstable because it needs to adjust its output to cancel the large noise. To ensure the stability

of the integration flow, we reparametrized the dynamics $g_{\theta}(\mathbf{x}_0, \mathbf{x}_t, t)$ as the following:

$$g_{\theta}(\mathbf{x}_0, \mathbf{x}_t, t) = a_t \mathbf{x}_t + b_t G_{\theta}(\mathbf{x}_0, \mathbf{x}_t, t). \quad (9)$$

where a_t and b_t are time-dependent scalar functions designed to modulate the contributions of \mathbf{x}_t and $G(\mathbf{x}_0, \mathbf{x}_t, t)$, respectively. This formulation introduces better flexibility in the evolution of the integration flow over time, particularly in scenarios where the straightforward application (Equation (8)) of integration may introduce instability, especially when the magnitudes of the intermediate state \mathbf{x}_t become large.

The goal of the training neural network is to accurately recover \mathbf{x}_0 from \mathbf{x}_t . Therefore, it is essential that:

$$g_{\theta}(\mathbf{x}_0, \mathbf{x}_t, t) \approx g(\mathbf{x}_0, \mathbf{x}_t, t) = \mathbf{x}_0 \quad (10)$$

However, $g_{\theta}(\mathbf{x}_0, \mathbf{x}_t, t)$ may not directly recover the true \mathbf{x}_0 accurately. We then employed an iterative refinement process. Starting with an initial $\mathbf{x}_0^{(0)} \sim \mathcal{N}(\mathbf{0}, \mathbf{I})$, the estimate is progressively refined using the following update rule:

$$\mathbf{x}_0^{(n+1)} = g_{\theta}(\mathbf{x}_0^{(n)}, \mathbf{x}_t, t) = a_t \mathbf{x}_t + b_t G_{\theta}(\mathbf{x}_0^{(n)}, \mathbf{x}_t, t) \quad (11)$$

Through this iterative process, the neural network will effectively minimize the discrepancy between the iteratively estimated $\mathbf{x}_0^{(n)}$ and the true initial state \mathbf{x}_0 with properly defined loss.

3.4. Theoretical justification

Theorem 1 (Stability): Let \mathbf{x}_0 represent the target state, \mathbf{x}_t represent an intermediate state, and t represent the time. Let $\mathbf{x}_0^{(n)}$ be an auxiliary estimate of \mathbf{x}_0 obtained through an iterative process. Consider the following two estimators:

(a) $\hat{\mathbf{x}}_0 = g'_{\theta}(\mathbf{x}_t, t)$, which estimates \mathbf{x}_0 based only on \mathbf{x}_t and t , analogous to $\mathbb{E}[\mathbf{x}_0 | \mathbf{x}_t]$;

(b) $\tilde{\mathbf{x}}_0 = g_{\theta}(\mathbf{x}_0^{(n)}, \mathbf{x}_t, t)$, which estimates \mathbf{x}_0 based on both $\mathbf{x}_0^{(n)}$, \mathbf{x}_t , and t , analogous to $\mathbb{E}[\mathbf{x}_0 | \mathbf{x}_t, \mathbf{x}_0^{(n)}]$.

Then, the estimator $\tilde{\mathbf{x}}_0$, which includes additional conditional information $\mathbf{x}_0^{(n)}$, provides a more accurate estimation of \mathbf{x}_0 compared to $\hat{\mathbf{x}}_0$, in terms of mean squared error (MSE). That is,

$$\mathbb{E}[\|\mathbf{x}_0 - \tilde{\mathbf{x}}_0\|^2] \leq \mathbb{E}[\|\mathbf{x}_0 - \hat{\mathbf{x}}_0\|^2] \quad (12)$$

Theorem 1 justifies that the estimator $\tilde{\mathbf{x}}_0$ is at least as accurate as $\hat{\mathbf{x}}_0$ under the same convex metric $d(\cdot, \cdot)$, illustrating that $\tilde{\mathbf{x}}_0 = g_{\theta}(\mathbf{x}_0^{(n)}, \mathbf{x}_t, t)$ provides a better or at least equal estimate compared to $\hat{\mathbf{x}}_0 = g'_{\theta}(\mathbf{x}_t, t)$.

Theorem 2 (Non-Intersection): Suppose that the neural network is sufficiently trained and θ^* is obtained, such that: $g_{\theta^*}(\mathbf{x}_0^{(n)}, \mathbf{x}_t, t) \equiv g(\mathbf{x}_0, \mathbf{x}_t, t)$ for any $t \in [0, T]$ and \mathbf{x}_0 sampled from p_{data} , and $v(\mathbf{x}_s, s)$ meets Lipschitz condition.

Then for any $t \in [0, T]$, the mapping $g_{\theta^*}(\mathbf{x}_0^{(n)}, \mathbf{x}_t, t) : \mathbb{R}^N \rightarrow \mathbb{R}^N$ is bi-Lipschitz. Namely, for any $\mathbf{x}_t, \mathbf{y}_t \in \mathbb{R}^N$

$$\begin{aligned} e^{-Lt} \|\mathbf{x}_t - \mathbf{y}_t\|_2 &\leq \|g_{\theta^*}(\mathbf{x}_0^{(n)}, \mathbf{x}_t, t) - g_{\theta^*}(\mathbf{y}_0^{(n)}, \mathbf{y}_t, t)\|_2 \\ &\leq e^{Lt} \|\mathbf{x}_t - \mathbf{y}_t\|_2. \end{aligned} \quad (13)$$

This implies that if given two different starting points, say $\mathbf{x}_T \neq \mathbf{y}_T$, by the bi-Lipschitz above, it can be concluded that $g_{\theta^*}(\mathbf{x}_0^{(n)}, \mathbf{x}_T, T) \neq g_{\theta^*}(\mathbf{y}_0^{(n)}, \mathbf{y}_T, T)$ i.e., $\mathbf{x}_0^{(n+1)} \neq \mathbf{y}_0^{(n+1)}$, which indicates the reverse path of Integration Flow does not intersect.

Theorem 3 (Integration Flow Optimality): Integration Flow is optimal for Flow Matching/Rectified Flow in the sense that any solution v to the continuous-time problem has a cost no better than the cost of the integrated approach. Therefore, a direct one-step method (via G) achieves the best possible value.

The proof of Theorems is presented in the Appendix B.

4. Integration Flow for different ODE-based generative models

In this section, we apply Integration Flow to three ODE-based generative models. More training settings can be seen in Table 1.

Integration Flow for Variance Exploding (VE) Diffusion Model. The forward process in the Variance Exploding (VE) diffusion model (Song et al., 2020b; Karras et al., 2022) adds noise to the data progressively. This process is described as:

$$\mathbf{x}_t = \mathbf{x}_0 + \sigma_t \epsilon, \quad t \in [0, T] \quad (14)$$

where $\mathbf{x}_0 \sim p_{\text{data}}$, σ_t denotes noise schedule that increases with time t , $\epsilon \sim \mathcal{N}(0, \mathbf{I})$. The reverse process aims to denoise the data by starting from a noisy sample \mathbf{x}_T and evolving it back to the clean data distribution p_{data} . This is achieved using the PF-ODEs, which model the continuous denoising process in the reverse direction. The PF-ODE is given by:

$$\frac{d\mathbf{x}_t}{dt} = -\frac{1}{2} \frac{d\sigma_t^2}{dt} \nabla_{\mathbf{x}_t} \log p_t(\mathbf{x}_t) \quad (15)$$

where $\nabla_{\mathbf{x}_t} \log p_t(\mathbf{x}_t)$ is the score function, representing the gradient of the log-probability of the data distribution $p_t(\mathbf{x}_t)$ at time t . We adopt the noise scheduler as $\sigma_{\min} \left(\frac{\sigma_{\max}}{\sigma_{\min}} \right)^{t/T}$,

Table 1. The different design choice of Integration Flow for different ODE-based methods. For training, we use the discrete time steps with $T = 1000$.

	VE(Song et al., 2020b)	Rectified Flow(Liu et al., 2022)	PFGM++(Xu et al., 2023)
Training			
Noise scheduler	$\sigma_{\min} \left(\frac{\sigma_{\max}}{\sigma_{\min}} \right)^{t/T}$	Linear interpolation, $\sigma = 0$	$R_t \mathbf{v}_t$, where $\sigma_t \sim p(\sigma_t)$, $r_t = \sigma_t \sqrt{D}$, $R_t \sim p_{r_t}(R)$, $\mathbf{v}_t = \frac{\mathbf{u}_t}{\ \mathbf{u}_t\ _2}$, $\mathbf{u}_t \sim \mathcal{N}(\mathbf{0}, \mathbf{I})$
Steps	$t \in [1, 2, \dots, T]$	$t \sim \text{Uniform}[0, 1]$	$t \in [1, 2, \dots, T]$
Network and preconditioning			
Architecture of F_θ	ADM	ADM	ADM
a_t	σ_{\min}/σ_t	0	σ_{\min}/R_t
b_t	$1 - \sigma_{\min}/\sigma_t$	1	$1 - \sigma_{\min}/R_t$
Sampling			
One step		$\mathbf{x}_0^{(\text{est})} = a_t \mathbf{x}_t + b_t G_\theta \left(\mathbf{x}_0^{(0)}, \mathbf{x}_t, t \right)$	
Multistep n		$\mathbf{x}_0^{(\text{est})} = a_t \mathbf{x}_t + b_t G_\theta \left(\mathbf{x}_0^{(n)}, \mathbf{x}_t, t \right)$	
Parameters			
	$\sigma_{\min} = 0.01$ $\sigma_{\max} = 50$	—	$\sigma_{\min} = 0.01$ $\sigma_{\max} = 50$ $D = 2048$

where noise increases exponentially over time from σ_{\min} to σ_{\max} , and time step t is designed as $t \in [1, 2, \dots, T]$. Therefore, the integration flow can be expressed as:

$$g_\theta(\mathbf{x}_0, \mathbf{x}_t, t) = \frac{\sigma_{\min}}{\sigma_t} \mathbf{x}_t + \left(1 - \frac{\sigma_{\min}}{\sigma_t} \right) G_\theta(\mathbf{x}_0, \mathbf{x}_t, t) \quad (16)$$

where the preconditioning terms are set as $a_t = \sigma_{\min}/\sigma_t$, and $b_t = 1 - \sigma_{\min}/\sigma_t$, which modulate the network’s response to different noise levels throughout training. The detailed derivation of the Integration Flow for VE diffusion model is in Appendix A.1.

Integration Flow for Rectified Flows. Rectified flows (Liu et al., 2022; Albergo & Vanden-Eijnden, 2022; Lipman et al., 2022) uses linear interpolation to connect the data distribution p_{data} and a standard normal distribution $p_{\mathbf{z}}$ by introducing a continuous forward process that smoothly transitions between these two distributions, which is defined as:

$$\mathbf{z}_t = (1 - t)\mathbf{x}_0 + t\mathbf{z}, \quad t \in [0, 1] \quad (17)$$

where \mathbf{x}_0 is a sample drawn from the data distribution p_{data} , \mathbf{z} is sampled from the standard normal distribution. Time step t is sampled from Uniform[0, 1]. Since this is a deterministic linear interpolation, there is no need of a noise scheduler. This interpolation ensures that at $t = 0$, it recovers the original data point, i.e., $\mathbf{z}_0 = \mathbf{x}_0$, and at $t = 1$, the point has been mapped entirely into the noise distribution, i.e., $\mathbf{z}_1 = \mathbf{z}$. Thus, a straight path is created between the data and the noise distributions.

Liu et al. (Liu et al., 2022) demonstrated that for $\mathbf{z}_0 \sim p_{\mathbf{x}}$, the dynamics of the following ODE produce marginals that

match the distribution of \mathbf{x}_t for any t :

$$\frac{d\mathbf{z}_t}{dt} = v(\mathbf{z}_t, t) \quad (18)$$

Since the interpolation ensures that $\mathbf{x}_1 = \mathbf{z}$, the forward ODE transports samples from the data distribution $p_{\mathbf{x}}$ to the noise distribution $p_{\mathbf{z}}$. To reverse this process, starting with $\mathbf{z}_1 \sim p_{\mathbf{z}}$, the ODE can be integrated backward from $t = 1$ to $t = 0$, ultimately reconstructing samples from the data distribution.

The integration flow of Rectified Flows can be expressed as:

$$\mathbf{x}_0 = g_\theta(\mathbf{x}_0, \mathbf{z}_t, t) = G_\theta(\mathbf{x}_0, \mathbf{z}_t, t) \quad (19)$$

Equivalent to $a_t = 0, b_t = 1$ in (9). The detailed derivation of Integration Flow for Rectified Flow is in the Appendix A.2. Moreover, Integration Flow supports Stochastic Interpolants (Albergo & Vanden-Eijnden, 2022) as well.

Integration Flow PFGM++. PFGM++ (Xu et al., 2023) is a generalization of PFGM(Xu et al., 2022) that embeds generative paths in a high-dimensional space. It reduces to PFGM when $D = 1$ and to diffusion models when $D \rightarrow \infty$.

In PFGM++, each data point $\mathbf{x} \in \mathbb{R}^N$ is augmented by additional variables $\mathbf{z} = (z_1, \dots, z_D) \in \mathbb{R}^D$, resulting in an augmented data representation $\tilde{\mathbf{x}} = (\mathbf{x}, \mathbf{z}) \in \mathbb{R}^{N+D}$. Due to the rotational symmetry of the electric field in the augmented space, the problem can be simplified by considering only the radial norm $r = \|\mathbf{z}\|_2$. This reduces the augmented data representation to $\tilde{\mathbf{x}} = (\mathbf{x}, r)$, where r acts as a scalar anchor variable.

PFGM++ uses the electric field $\mathbf{E}(\tilde{\mathbf{x}})$ to drive the dynamics of the generative process. Using the radial symmetry of the

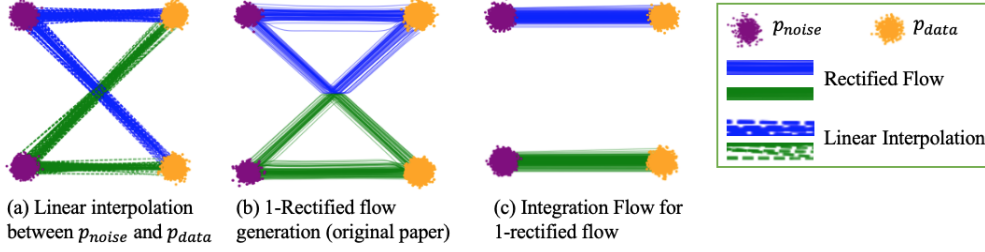


Figure 2. Rectified flow process. (a)-(b) Flow rewires trajectories of original rectified flow, regenerated from (Liu et al., 2022). (c) Straigten flows of Integration Flow based 1-rectified flow.

electric field, the backward ODE that governs the generative process can be expressed as:

$$\frac{d\mathbf{x}}{dr} = \frac{\mathbf{E}(\tilde{\mathbf{x}})_{\mathbf{x}}}{E(\tilde{\mathbf{x}})_r} \quad (20)$$

By solving this ODE in reverse, one can transport points from the high dimensional augmented space back to the original data space, completing the generative process.

PFGM++ introduces an alignment method to transfer hyperparameters from diffusion models (where $D \rightarrow \infty$) to finite-dimensional settings. The alignment is based on the relationship:

$$r = \sigma\sqrt{D} \quad (21)$$

This formula ensures that the phases of the intermediate distributions in PFGM++ are aligned with those of diffusion models. The relation allows transferring finely-tuned hyperparameters like σ_{\max} and $p(\sigma)$ from diffusion models to PFGM++ using:

$$r_{\max} = \sigma_{\max}\sqrt{D}, \quad p(r) = \frac{p(\sigma = r/\sqrt{D})}{\sqrt{D}} \quad (22)$$

Further, (Xu et al., 2023) showed

$$\frac{d\mathbf{x}}{dr} = \frac{d\mathbf{x}}{d\sigma} \quad (23)$$

where σ changes with time. Thus, we adopt the noise scheduler the same as in VE case. And the perturbation to the original data \mathbf{x}_0 can be written as:

$$\mathbf{x}_t = \mathbf{x}_0 + R_t \mathbf{v}_t \quad (24)$$

Specifically, for each data point \mathbf{x}_0 , a radius R_t is sampled from the distribution $p_{r_t}(R)$ (See Appendix B in (Xu et al., 2023) to sample R_t). To introduce random perturbations, uniform angles are sampled by first drawing from a standard multivariate Gaussian, $\mathbf{u}_t \sim \mathcal{N}(\mathbf{0}, \mathbf{I})$, and then normalizing these vectors to obtain unit direction vectors $\mathbf{v}_t = \frac{\mathbf{u}_t}{\|\mathbf{u}_t\|_2}$. This perturbation acts as a forward process in PFGM++, analogous to the forward process in diffusion models.

The Integration Flow $g_{\theta}(\mathbf{x}_0, \mathbf{x}_t, \sigma_t)$ of PFGM++ can be expressed as:

$$g_{\theta}(\mathbf{x}_0, \mathbf{x}_t, t) = \frac{\sigma_{\min}}{R_t} \mathbf{x}_t + (1 - \frac{\sigma_{\min}}{R_t}) G_{\theta}(\mathbf{x}_0, \mathbf{x}_t, t) \quad (25)$$

with $a_t = \sigma_{\min}/R_t$ and $b_t = 1 - \sigma_{\min}/R_t$, and the detailed derivation of a_t, b_t is shown in Appendix A.3.

5. Experiments

To evaluate our method for image generation, we train several Integration Flow Models on CIFAR-10 (Krizhevsky et al., 2009) and ImageNet 64x64 (Deng et al., 2009) and benchmark their performance with competing methods in the literature. Results are compared according to Frechet Inception Distance (FID, Heusel et al. (2017)), which is computed between 50K generated samples and the whole training set. The training and sampling algorithm can be found in the Appendix A.

5.1. Implementation Details

Architecture. We employed the ADM architecture (Dhariwal & Nichol, 2021) for the implementation of Integration Flow. For CIFAR-10, the base channel dimension is set to 128 and is multiplied by 1,2,2,2 in four stages. For ImageNet 64x64, the base channel dimension is set to 192 and is multiplied by 1,2,3,4 in four stages. For both datasets, we used three residual blocks per stage and set the Dropout (Srivastava et al., 2014) rate to 0.3. We also used cross-attention modules at both the 16x16 resolution and the 8x8 resolution, where the conditioning image $\mathbf{x}_0^{(n)}$ is integrated into the network. The models for CIFAR-10 are unconditional, but the models for ImageNet are conditioned on class labels.

Loss function Inspired by (Song & Dhariwal, 2023), we adopt the Pseudo-Huber metric family (Charbonnier et al., 1997) as the loss function, defined as

$$d(\mathbf{x}, \mathbf{y}) = \sqrt{\|\mathbf{x} - \mathbf{y}\|_2^2 + c^2} - c \quad (26)$$

where c is an adjustable hyperparameter. The Pseudo-Huber metric is more robust to outliers compared to the squared ℓ_2



Figure 3. One-step samples from Integration Flow. Top: ImageNet; Bottom: CIFAR-10. (a) and (d): 1-rectified flow with FID 4.35 and 3.36; (b) and (e): VE with FID 4.09 and 2.86; (c) and (f): PFGM++ with FID 4.15 and 2.91

loss metric because it imposes a smaller penalty for large errors, while still behaving similarly to the squared ℓ_2 loss metric for smaller errors. We set $c = 0.00016$ for VE, $c = 0.0001$ for Rectified Flow, and $c = 0.00016$ for PFGM++, respectively.

Other settings. We used Adam for all of our experiments. For VE and PFGM++, we set $T=1000$ for CIFAR10 and $T=2000$ for ImageNet. For all three Integration Flow models, we trained 400,000 iterations with a constant learning rate of 0.0002 and batch size of 128 for CIFAR 10 and trained 600,000 iterations with a constant learning rate of 0.0001 and batch size of 1024 for ImageNet. All experiments used the exponential moving average (EMA) of the weights during training with a decay factor of 0.9999. All models are trained on NVIDIA H100 DGX.

5.2. Comparison to SOTA

We compare our models against the state-of-the-art generative models on CIFAR-10 and ImageNet 64X64. The quantitative results are summarized in Table 2 and Table 3. For VE, Integration Flow achieved performances that are comparable to the state-of-the-art on both datasets. Specifically, Integration Flow one-step generation obtains FIDs of 2.86 for CIFAR-10 and 4.09 for ImageNet.

For Rectified Flow, the one-step generation with Integration Flow has reached FIDs of 3.36 for CIFAR10 and 4.35 for ImageNet without reflow, which is the state-of-the-art performance in the Rectified Flow. Generally, the Rectified Flow needs to be applied at least twice (Reflow) to obtain a reasonable one-step generation performance (Liu et al., 2022; 2023). The Integration Flow one-step generation has a better (CIFAR10) or comparable (ImageNet) performance compared to the best results of Reflow. As shown in Figure 2, the flow has already become exactly straight for

Table 2. Performance evaluation of unconditional samples on CIFAR-10

Method	NFE(↓)	FID(↓)	IS(↑)
Diffusion Models - Fast Samplers & Distillation			
DDIM (Song et al., 2020a)	10	13.36	
DPM-solver-fast (Lu et al., 2022)	10	4.70	
3-DEIS (Zhang & Chen, 2022)	10	4.17	
UniPC (Zhao et al., 2023)	10	3.87	
DFNO (LPIPS) (Zheng et al., 2023)	1	3.78	
Knowledge Distillation (Luhman & Luhman, 2021)	1	9.36	
TRACT (Berthelot et al., 2023)	1	3.78	
	2	3.32	
Diff-Instruct (Luo et al., 2023)	1	4.53	9.89
Diffusion Models - Direct Generation			
Score SDE (Song et al., 2020b)	2000	2.38	9.83
Score SDE (deep) (Song et al., 2020b)	2000	2.20	9.89
DDPM (Ho et al., 2020)	1000	3.17	9.46
LSGM (Vahdat et al., 2021)	147	2.10	
EDM (Karras et al., 2022)	35	2.04	9.84
EDM-G++ (Kim et al., 2022)	35	1.77	
GAN Models			
BigGAN (Brock et al., 2018)	1	14.7	9.22
StyleGAN2 (Karras et al., 2020a)	1	8.32	9.21
StyleGAN2-ADA (Karras et al., 2020b)	1	2.92	9.83
Consistency Models			
CD (LPIPS) (Song et al., 2023)	1	3.55	9.48
	2	2.93	9.75
CT (LPIPS) (Song et al., 2023)	1	8.70	8.49
	2	5.83	8.85
iCT (Song & Dhariwal, 2023)	1	2.83	9.54
	2	2.46	9.80
iCT-deep (Song & Dhariwal, 2023)	1	2.51	9.76
	2	2.24	9.89
CTM (Kim et al., 2024)	1	5.19	
CTM (Kim et al., 2024) + GAN	1	2.39	
Rectified Flows			
1-Rectified flow (Liu et al., 2022)	1	378	1.03
1-Rectified flow (+distill) (Liu et al., 2022)	1	6.18	9.08
2-Rectified Flow (+distill)(Liu et al., 2022)	1	4.85	9.01
2-Rectified flow++ (Lee et al., 2024)	1	3.38	
	2	2.76	
CFM(Yang et al., 2024)	2	5.34	8.70
Other Generative Models			
PFGM (Xu et al., 2022)	110	2.35	9.68
PFGM++ (Xu et al., 2023)	110	2.35	9.68
Integration Flow Models			
VE	1	2.86	9.56
	2	2.62	9.76
1-Rectified Flow	1	3.36	9.49
	2	2.75	
PFGM++, D=2048	1	2.91	

Integration Flow-based 1-rectified flow. This explains why Integration Flow-based 1-rectified flow can achieve good results as Reflow did.

For PFGM++, Integration Flow one-step generation has reached FIDs of 2.91 for CIFAR10 and 4.15 for ImageNet. We are the first to show that the PFGM++ can also achieve one-step generation with good performance.

6. Discussion

A key achievement of Integration Flow is its ability to solve different ODE-based models using a single framework, ad-

Table 3. Performance evaluation of class-conditional samples on ImageNet 64x64.

Method	NFE(↓)	FID(↓)	Prec.(↑)	Rec.(↑)
Diffusion Models - Fast Samplers & Distillation				
DDIM (Song et al., 2020a)	50	13.7	0.65	0.56
	10	18.3	0.60	0.49
DPM solver (Lu et al., 2022)	10	7.93		
	20	3.42		
DEIS (Zhang & Chen, 2022)	10	6.65		
	20	3.10		
DFNO (LPIPS) (Zheng et al., 2023)	1	7.83	0.61	
TRACT (Berthelot et al., 2023)	1	7.43		
	2	4.97		
BOOT (Gu et al., 2023)	1	16.3	0.68	0.36
Diff-Instruct (Luo et al., 2023)	1	5.57		
PD (LPIPS) (Song et al., 2023)	1	7.88	0.66	0.63
	2	5.74	0.67	0.65
Diffusion Models - Direct Generation				
RIN (Jabri et al., 2022)	1000	1.23		
DDPM (Ho et al., 2020)	250	11.0	0.67	0.58
iDDPM (Nichol & Dhariwal, 2021)	250	2.92	0.74	0.62
ADM (Dhariwal & Nichol, 2021)	250	2.07	0.74	0.63
EDM (Karras et al., 2022)	511	1.36		
GAN Models				
BigGAN-deep (Brock et al., 2018)	1	4.06	0.79	0.48
Consistency Models				
CT (LPIPS) (Song et al., 2023)	1	13.0	0.71	0.47
	2	11.1	0.69	0.56
iCT (Song & Dhariwal, 2023)	1	4.02	0.70	0.63
	2	3.20	0.73	0.63
iCT-deep (Song & Dhariwal, 2023)	1	3.25	0.72	0.63
	2	2.77	0.74	0.62
CTM + GAN* (Kim et al., 2024)	1	1.92		0.57
Multistep-CD (Heek et al., 2024)	1	4.3		
	2	2.0		
Multistep-CT(Heek et al., 2024)	1	7.2		
	2	2.7		
Rectified Flows				
2-Rectified flow++ (Lee et al., 2024)	1	4.31		
	2	3.64		
Integration Flow Models				
VE	1	4.09		
	2	3.28		
1-Rectified Flow	1	4.35		
	2	3.68		
PFGM++, D=2048	1	4.15		

ressing a significant challenge that prior models struggled with. For example, two important generative models, the Rectified Flow and diffusion model, are not unified, but Integration Flow can successfully integrate them. This not only simplifies the landscape of ODE-based generative models but also expands their applicability, making them easier to implement across different domains.

Although Integration Flow has achieved the best performance on one-step generation for Rectified Flow and PFGM++, the performance of Integration Flow for VE is still slightly underperformed compared to the current state-of-the-art. We hypothesize that this small performance gap may be attributed to suboptimal hyperparameters in the loss function. Due to limited computation resources, we are not able to search for the best hyperparameter.

Additionally, we recognize that different noise schedulers can significantly impact the model’s performance. The noise scheduling strategy plays a crucial role in the training dynamics and final performance of the model. We plan to investigate more complex schedulers in future work.

Furthermore, same as DDDM, Integration Flow also needs additional memory consumption during training. One solution is to store $\mathbf{x}_0^{(n)}$ in a buffer or on disk instead of on the GPU. However, this approach will introduce additional overhead during training due to the need to transfer data back to the GPU. We will fix this in our future work.

Impact Statement

This paper presents work whose goal is to advance the field of Machine Learning. There are many potential societal consequences of our work, none of which we feel must be specifically highlighted here.

References

- Albergo, M. S. and Vanden-Eijnden, E. Building normalizing flows with stochastic interpolants. *arXiv preprint arXiv:2209.15571*, 2022.
- Berthelot, D., Autef, A., Lin, J., Yap, D. A., Zhai, S., Hu, S., Zheng, D., Talbot, W., and Gu, E. Tract: Denoising diffusion models with transitive closure time-distillation. *arXiv preprint arXiv:2303.04248*, 2023.
- Bortoli, V. D., Thornton, J., Heng, J., and Doucet, A. Diffusion schrödinger bridge with applications to score-based generative modeling, 2023.
- Brock, A., Donahue, J., and Simonyan, K. Large scale gan training for high fidelity natural image synthesis. *arXiv preprint arXiv:1809.11096*, 2018.
- Charbonnier, P., Blanc-Feraud, L., Aubert, G., and Barlaud, M. Deterministic edge-preserving regularization in computed imaging. *IEEE Transactions on Image Processing*, 6(2):298–311, 1997. doi: 10.1109/83.551699.
- Chen, R. T., Rubanova, Y., Bettencourt, J., and Duvenaud, D. K. Neural ordinary differential equations. *Advances in neural information processing systems*, 31, 2018.
- Deng, J., Dong, W., Socher, R., Li, L.-J., Li, K., and Fei-Fei, L. Imagenet: A large-scale hierarchical image database. In *2009 IEEE conference on computer vision and pattern recognition*, pp. 248–255. Ieee, 2009.
- Dhariwal, P. and Nichol, A. Diffusion models beat gans on image synthesis. *Advances in neural information processing systems*, 34:8780–8794, 2021.
- Gholami, A., Keutzer, K., and Biros, G. Anode: Unconditionally accurate memory-efficient gradients for neural odes. *arXiv preprint arXiv:1902.10298*, 2019.
- Gu, J., Zhai, S., Zhang, Y., Liu, L., and Susskind, J. Boot: Data-free distillation of denoising diffusion models with bootstrapping. *arXiv preprint arXiv:2306.05544*, 2023.
- Heek, J., Hoogeboom, E., and Salimans, T. Multistep consistency models. *arXiv preprint arXiv:2403.06807*, 2024.
- Heusel, M., Ramsauer, H., Unterthiner, T., Nessler, B., and Hochreiter, S. Gans trained by a two time-scale update rule converge to a local nash equilibrium. *Advances in neural information processing systems*, 30, 2017.
- Ho, J. and Salimans, T. Classifier-free diffusion guidance, 2022.
- Ho, J., Jain, A., and Abbeel, P. Denoising diffusion probabilistic models. *Advances in neural information processing systems*, 33:6840–6851, 2020.
- Jabri, A., Fleet, D., and Chen, T. Scalable adaptive computation for iterative generation. *arXiv preprint arXiv:2212.11972*, 2022.
- Karras, T., Laine, S., Aittala, M., Hellsten, J., Lehtinen, J., and Aila, T. Analyzing and improving the image quality of stylegan. In *Proceedings of the IEEE/CVF conference on computer vision and pattern recognition*, pp. 8110–8119, 2020a.
- Karras, T., Laine, S., Aittala, M., Hellsten, J., Lehtinen, J., and Aila, T. Analyzing and improving the image quality of stylegan. In *Proceedings of the IEEE/CVF conference on computer vision and pattern recognition*, pp. 8110–8119, 2020b.
- Karras, T., Aittala, M., Aila, T., and Laine, S. Elucidating the design space of diffusion-based generative models. *Advances in Neural Information Processing Systems*, 35: 26565–26577, 2022.
- Kim, D., Kim, Y., Kwon, S. J., Kang, W., and Moon, I.-C. Refining generative process with discriminator guidance in score-based diffusion models. *arXiv preprint arXiv:2211.17091*, 2022.
- Kim, D., Lai, C.-H., Liao, W.-H., Murata, N., Takida, Y., Uesaka, T., He, Y., Mitsufuji, Y., and Ermon, S. Consistency trajectory models: Learning probability flow ode trajectory of diffusion, 2024.
- Kong, Z., Ping, W., Huang, J., Zhao, K., and Catanzaro, B. Diffwave: A versatile diffusion model for audio synthesis. In *International Conference on Learning Representations*, 2021. URL <https://openreview.net/forum?id=a-xFK8Ymz5J>.

- Krizhevsky, A., Hinton, G., et al. Learning multiple layers of features from tiny images. 2009.
- Lee, S., Lin, Z., and Fanti, G. Improving the training of rectified flows. *arXiv preprint arXiv:2405.20320*, 2024.
- Lipman, Y., Chen, R. T., Ben-Hamu, H., Nickel, M., and Le, M. Flow matching for generative modeling. *arXiv preprint arXiv:2210.02747*, 2022.
- Liu, X., Gong, C., and Liu, Q. Flow straight and fast: Learning to generate and transfer data with rectified flow. *arXiv preprint arXiv:2209.03003*, 2022.
- Liu, X., Zhang, X., Ma, J., Peng, J., et al. InstafLOW: One step is enough for high-quality diffusion-based text-to-image generation. In *The Twelfth International Conference on Learning Representations*, 2023.
- Lu, C., Zhou, Y., Bao, F., Chen, J., Li, C., and Zhu, J. Dpm-solver: A fast ode solver for diffusion probabilistic model sampling in around 10 steps. *Advances in Neural Information Processing Systems*, 35:5775–5787, 2022.
- Luhman, E. and Luhman, T. Knowledge distillation in iterative generative models for improved sampling speed. *arXiv preprint arXiv:2101.02388*, 2021.
- Luo, W., Hu, T., Zhang, S., Sun, J., Li, Z., and Zhang, Z. Diff-instruct: A universal approach for transferring knowledge from pre-trained diffusion models. *arXiv preprint arXiv:2305.18455*, 2023.
- Nichol, A. Q. and Dhariwal, P. Improved denoising diffusion probabilistic models. In *International Conference on Machine Learning*, pp. 8162–8171. PMLR, 2021.
- Popov, V., Vovk, I., Gogoryan, V., Sadekova, T., Kudinov, M., and Wei, J. Diffusion-based voice conversion with fast maximum likelihood sampling scheme, 2022.
- Rombach, R., Blattmann, A., Lorenz, D., Esser, P., and Ommer, B. High-resolution image synthesis with latent diffusion models. In *Proceedings of the IEEE/CVF conference on computer vision and pattern recognition*, pp. 10684–10695, 2022.
- Saharia, C., Chan, W., Saxena, S., Li, L., Whang, J., Denton, E. L., Ghasemipour, K., Gontijo Lopes, R., Karagol Ayan, B., Salimans, T., et al. Photorealistic text-to-image diffusion models with deep language understanding. *Advances in Neural Information Processing Systems*, 35: 36479–36494, 2022.
- Sauer, A., Karras, T., Laine, S., Geiger, A., and Aila, T. Stylegan-t: Unlocking the power of gans for fast large-scale text-to-image synthesis, 2023. URL <https://arxiv.org/abs/2301.09515>.
- Song, J., Meng, C., and Ermon, S. Denoising diffusion implicit models. *arXiv preprint arXiv:2010.02502*, 2020a.
- Song, Y. and Dhariwal, P. Improved techniques for training consistency models. *arXiv preprint arXiv:2310.14189*, 2023.
- Song, Y., Sohl-Dickstein, J., Kingma, D. P., Kumar, A., Ermon, S., and Poole, B. Score-based generative modeling through stochastic differential equations. *arXiv preprint arXiv:2011.13456*, 2020b.
- Song, Y., Dhariwal, P., Chen, M., and Sutskever, I. Consistency models. *arXiv preprint arXiv:2303.01469*, 2023.
- Srivastava, N., Hinton, G., Krizhevsky, A., Sutskever, I., and Salakhutdinov, R. Dropout: a simple way to prevent neural networks from overfitting. *The journal of machine learning research*, 15(1):1929–1958, 2014.
- Vahdat, A., Kreis, K., and Kautz, J. Score-based generative modeling in latent space. *Advances in Neural Information Processing Systems*, 34:11287–11302, 2021.
- Xu, Y., Liu, Z., Tegmark, M., and Jaakkola, T. Poisson flow generative models. *Advances in Neural Information Processing Systems*, 35:16782–16795, 2022.
- Xu, Y., Liu, Z., Tian, Y., Tong, S., Tegmark, M., and Jaakkola, T. Pfgm++: Unlocking the potential of physics-inspired generative models. In *International Conference on Machine Learning*, pp. 38566–38591. PMLR, 2023.
- Yang, L., Zhang, Z., Zhang, Z., Liu, X., Xu, M., Zhang, W., Meng, C., Ermon, S., and Cui, B. Consistency flow matching: Defining straight flows with velocity consistency. *arXiv preprint arXiv:2407.02398*, 2024.
- Zhang, D., Wang, J., and Luo, F. Directly denoising diffusion model. *arXiv preprint arXiv:2405.13540*, 2024.
- Zhang, Q. and Chen, Y. Fast sampling of diffusion models with exponential integrator. *arXiv preprint arXiv:2204.13902*, 2022.
- Zhao, W., Bai, L., Rao, Y., Zhou, J., and Lu, J. Unipc: A unified predictor-corrector framework for fast sampling of diffusion models. *arXiv preprint arXiv:2302.04867*, 2023.
- Zheng, H., Nie, W., Vahdat, A., Aizzadenesheli, K., and Anandkumar, A. Fast sampling of diffusion models via operator learning. In *International Conference on Machine Learning*, pp. 42390–42402. PMLR, 2023.

A. Derivation of Integration Flow Algorithms

A.1. Integration Flow for VE diffusion models

The PF-ODE of VE diffusion models is formulated as:

$$\frac{d\mathbf{x}_t}{dt} = -\frac{1}{2} \frac{d\sigma_t^2}{dt} \nabla_{\mathbf{x}_t} \log p_t(\mathbf{x}_t) \quad (27)$$

We do the reversed time integration on both sides over the interval $[0, t]$:

$$\int_t^0 \frac{d\mathbf{x}_s}{ds} = \int_t^0 -\frac{1}{2} \frac{d\sigma_t^2}{dt} \nabla_{\mathbf{x}_t} \log p_t(\mathbf{x}_t) \quad (28)$$

and obtain:

$$\mathbf{x}_0 - \mathbf{x}_t = V(\mathbf{x}_0, 0) - V(\mathbf{x}_t, t) = -G(\mathbf{x}_0, \mathbf{x}_t, t) \quad (29)$$

Thus:

$$\mathbf{x}_0 = \mathbf{x}_t - G(\mathbf{x}_0, \mathbf{x}_t, t) = g(\mathbf{x}_0, \mathbf{x}_t, t) \quad (30)$$

For stable training purpose, we rewrite $g(\mathbf{x}_0, \mathbf{x}_t, t)$ as following:

$$g(\mathbf{x}_0, \mathbf{x}_t, t) = \mathbf{x}_t - G(\mathbf{x}_0, \mathbf{x}_t, t) = \kappa(\sigma_t) \mathbf{x}_t + (1 - \kappa(\sigma_t)) * \left[\mathbf{x}_t - \frac{1}{1 - \kappa(\sigma_t)} G(\mathbf{x}_0, \mathbf{x}_t, t) \right] \quad (31)$$

We define the neural network as:

$$g_{\theta}(\mathbf{x}_0, \mathbf{x}_t, t) = \kappa(\sigma_t) \mathbf{x}_t + \frac{1}{1 - \kappa(\sigma_t)} G_{\theta}(\mathbf{x}_0, \mathbf{x}_t, t), \quad (32)$$

where we use neural network to estimate the value of $\mathbf{x}_t - (1 - \kappa(\sigma_t)) G(\mathbf{x}_0, \mathbf{x}_t, t)$.

For VE Diffusion model, we have $a(\sigma_t) = \kappa(\sigma_t)$ and $b(\sigma_t) = 1 - \kappa(\sigma_t)$. There are a few choices for the design of $\kappa(\sigma_t)$, such as $\kappa(\sigma_t) = \frac{\sigma_{\text{data}}}{\sigma_t + \sigma_{\text{data}}}$, $\kappa(\sigma_t) = \frac{\sigma_{\text{data}}^2}{\sigma_t^2 + \sigma_{\text{data}}^2}$, which are in a manner of (Karras et al., 2022). We set $\kappa(\sigma_t) = \frac{\sigma_{\min}}{\sigma_t}$ in this work.

Algorithm 1 Integration Flow Training Algorithm for VE Diffusion Model

Input: p_{data}, T , model parameter θ , initialize $\mathbf{x}_0^{(0)} \sim \mathcal{N}(\mathbf{0}, \mathbf{I})$, epoch $n \leftarrow 0$

repeat

 Sample $\mathbf{x}_0 \sim p_{\text{data}}, t \sim \mathcal{U}[1, T]$ and $\epsilon \sim \mathcal{N}(\mathbf{0}, \mathbf{I})$

$\mathbf{x}_t = \mathbf{x}_0 + \sigma_t \epsilon$

$\mathbf{x}_0^{(n+1)} \leftarrow g_{\theta}(\mathbf{x}_0^{(n)}, \mathbf{x}_t, t)$

$\mathcal{L}_{\text{IFM}}^{(n+1)}(\theta) \leftarrow d(\mathbf{x}_0^{(n+1)}, \mathbf{x}_0)$

$\theta \leftarrow \theta - \eta \nabla_{\theta} \mathcal{L}(\theta)$

$n \leftarrow n + 1$

until convergence

A.2. Integration Flow for Rectified Flow

To analyze the integration flow associated with this process, we consider the derivative of \mathbf{z}_t with respect to time $t \in [0, 1]$:

$$\frac{d\mathbf{z}_t}{dt} = v(\mathbf{z}_t, t)$$

Integrating the both side, we obtain:

Algorithm 2 Integration Flow Sampling Algorithm for VE Diffusion Model

Input: T , trained model parameter θ , sampling step k , initialize $\mathbf{x}_0^{(0)} \sim \mathcal{N}(\mathbf{0}, \mathbf{I})$, $\mathbf{x}_T \sim \mathcal{N}(\mathbf{0}, \mathbf{I})$
 $\mathbf{x}_T = \sigma_{\max} \mathbf{x}_T$
for $k = 0$ **to** $k - 1$ **do**
 $\mathbf{x}_0^{(k+1)} \leftarrow g_{\theta}(\mathbf{x}_0^{(k)}, \mathbf{x}_T, T)$
end for
Output: $\mathbf{x}_0^{(k+1)}$

$$\int_0^1 \frac{d\mathbf{z}_s}{ds} ds = \mathbf{z} - \mathbf{x}_0.$$

This confirms that the total change over the entire path from $t = 0$ to $t = 1$ is simply the difference between the endpoints \mathbf{z} and \mathbf{x}_0 .

For any intermediate time $t \in [0, 1]$, reserve-time integration over $[0, t]$ yields:

$$\int_t^0 \frac{d\mathbf{z}_s}{ds} ds = \mathbf{x}_0 - \mathbf{z}_t = V(\mathbf{x}_0, 0) - V(\mathbf{x}_t, t) = -G(\mathbf{x}_0, \mathbf{z}_t, t), \quad (33)$$

where we define the accumulated change $G(\mathbf{x}_0, \mathbf{z}_t, t)$ as:

$$G(\mathbf{x}_0, \mathbf{z}_t, t) = \mathbf{z}_t - \mathbf{x}_0. \quad (34)$$

Substituting the expression for \mathbf{z}_t , we have:

$$\mathbf{z}_t - \mathbf{x}_0 = [(1-t)\mathbf{x}_0 + t\mathbf{z}] - \mathbf{x}_0 = t(\mathbf{z} - \mathbf{x}_0). \quad (35)$$

Thus, the accumulated change is proportional to the time parameter t and the difference $\mathbf{z} - \mathbf{x}_0$:

$$G(\mathbf{x}_0, \mathbf{z}_t, t) = t(\mathbf{z} - \mathbf{x}_0). \quad (36)$$

Rearranging this expression allows us to solve for $\mathbf{z} - \mathbf{x}_0$:

$$\mathbf{z} - \mathbf{x}_0 = \frac{G(\mathbf{x}_0, \mathbf{z}_t, t)}{t}. \quad (37)$$

This relationship indicates that the total accumulated change $\mathbf{z} - \mathbf{x}_0$ can be expressed in terms of the accumulated change $G(\mathbf{x}_0, \mathbf{z}_t, t)$ scaled by $1/t$.

We can now define the Integration Flow of the Rectified Flow process by expressing \mathbf{x}_0 in terms of $G(\mathbf{x}_0, \mathbf{z}_t, t)$ and the endpoint \mathbf{z} :

$$\mathbf{x}_0 = \mathbf{z} - \frac{G(\mathbf{x}_0, \mathbf{z}_t, t)}{t} = g(\mathbf{x}_0, \mathbf{z}_t, t). \quad (38)$$

In practice, since \mathbf{z} is deterministic, it can be absorbed into the neural network; for stable training, we take $G(\mathbf{x}_0, \mathbf{z}_t, t)/t$ as a whole.

Thus, we have:

$$g_{\theta}(\mathbf{x}_0, \mathbf{z}_t, t) = G_{\theta}(\mathbf{x}_0, \mathbf{z}_t, t),$$

which indicates $a_t = 0$ and $b_t = 1$.

By employing this enhanced dynamic model within the Rectified Flow framework, we can achieve a more accurate and stable reconstruction of the initial data point \mathbf{x}_0 , facilitating effective generative modeling and data synthesis.

Algorithm 3 Integration Flow Training Algorithm for Rectified Flows

Input: couple $(\mathbf{x}_0, \mathbf{z})$ from p_{data} and $p_{\mathbf{z}}$, respectively; model parameter θ , initialize $\mathbf{x}_0^{(0)} \sim \mathcal{N}(\mathbf{0}, \mathbf{I})$, epoch $n \leftarrow 0$
repeat
 Sample $\mathbf{x}_0 \sim p_{\text{data}}, t \sim \text{Uniform}[0, 1]$
 $\mathbf{z}_t = (1 - t)\mathbf{x}_0 + t\mathbf{z}$
 $\mathbf{x}_0^{(n+1)} \leftarrow g_\theta(\mathbf{x}_0^{(n)}, \mathbf{z}_t, t)$
 $\mathcal{L}_{\text{IFM}}^{(n+1)}(\theta) \leftarrow d(\mathbf{x}_0^{(n+1)}, \mathbf{x}_0)$
 $\theta \leftarrow \theta - \eta \nabla_\theta \mathcal{L}(\theta)$
 $n \leftarrow n + 1$
until convergence

Algorithm 4 Integration Flow Sampling Algorithm for Rectified Flows

Input: $t = 1$, trained model parameter θ , draw $\mathbf{z} \sim p_{\mathbf{z}}$, initialize $\mathbf{x}_0^{(0)} \sim \mathcal{N}(\mathbf{0}, \mathbf{I})$, sampling step k , initialize $\mathbf{x}_0^{(0)} \sim \mathcal{N}(\mathbf{0}, \mathbf{I})$
for $k = 0$ **to** $k - 1$ **do**
 $\mathbf{x}_0^{(k+1)} \leftarrow g_\theta(\mathbf{x}_0^{(k)}, \mathbf{z}, t)$
end for
Output: $\mathbf{x}_0^{(k+1)}$

A.3. Integration Flow for PFGM++

The backward ODE of PFGM++ is characterized as:

$$\frac{d\mathbf{x}}{dr} = \frac{\mathbf{E}(\tilde{\mathbf{x}})_{\mathbf{x}}}{E(\tilde{\mathbf{x}})_r} \quad (39)$$

Since (Xu et al., 2023) showed that $d\mathbf{x}/dr = d\mathbf{x}/d\sigma$, where σ changes with time.

We modify the (39) as:

$$\frac{d\mathbf{x}}{dt} = \frac{d\mathbf{x}}{dr} \frac{d\sigma_t}{dt} = \frac{\mathbf{E}(\tilde{\mathbf{x}})_{\mathbf{x}}}{E(\tilde{\mathbf{x}})_r} \frac{d\sigma_t}{dt} \quad (40)$$

We do the reversed time integration on both sides with respect to t over the interval $[0, t]$, leading to:

$$\int_t^0 \frac{d\mathbf{x}}{dt} dt = \int_t^0 \frac{\mathbf{E}(\tilde{\mathbf{x}})_{\mathbf{x}}}{E(\tilde{\mathbf{x}})_r} \frac{d\sigma_t}{dt} dt, \quad (41)$$

which is equivalent to:

$$\mathbf{x}_0 - \mathbf{x}_t = V(\mathbf{x}_0, 0) - V(\mathbf{x}_t, t) = -G(\mathbf{x}_0, \mathbf{x}_t, t) \quad (42)$$

Rearranging the equation, we express the initial data point in terms of the integration flow:

$$\mathbf{x}_0 = \mathbf{x}_t - G(\mathbf{x}_0, \mathbf{x}_t, t) = g(\mathbf{x}_0, \mathbf{x}_t, t).$$

For stable training purpose, we rewrite $g(\mathbf{x}_0, \mathbf{x}_t, t)$ as following:

$$g(\mathbf{x}_0, \mathbf{x}_t, t) = \mathbf{x}_t - G(\mathbf{x}_0, \mathbf{x}_t, t) = a_t \mathbf{x}_t + (1 - a_t) \left[\mathbf{x}_t - \frac{1}{1 - a_t} G(\mathbf{x}_0, \mathbf{x}_t, t) \right] \quad (43)$$

Since $\mathbf{x}_t = \mathbf{x}_0 + R_t \mathbf{v}_t$, inspired by the settings of a_t, b_t in VE case of diffusion model, we set $a_t = \sigma_{\min}/R_t, b_t = 1 - a_t = 1 - \sigma_{\min}/R_t$.

Algorithm 5 Integration Flow Training Algorithm for PFGM++

Input: p_{data}, T , model parameter θ , initialize $\mathbf{x}_0^{(0)} \sim \mathcal{N}(\mathbf{0}, \mathbf{I})$, epoch $n \leftarrow 0$

repeat

 Sample $\mathbf{x}_0 \sim p_{\text{data}}, t \sim \mathcal{U}[1, T]$

 Sample R_t, \mathbf{v}_t where:

$R_t = \sigma_t \sqrt{D}, \quad R_t \sim p_{r_t}(R)$

$\mathbf{v}_t = \frac{\mathbf{u}_t}{\|\mathbf{u}_t\|_2}, \quad \mathbf{u}_t \sim \mathcal{N}(\mathbf{0}, \mathbf{I})$

 Compute $\mathbf{x}_t = \mathbf{x}_0 + R_t \mathbf{v}_t$

$\mathbf{x}_0^{(n+1)} \leftarrow g_\theta(\mathbf{x}_0^{(n)}, \mathbf{x}_t, t)$

$\mathcal{L}_{\text{IFM}}^{(n+1)}(\theta) \leftarrow d(\mathbf{x}_0^{(n+1)}, \mathbf{x}_0)$

$\theta \leftarrow \theta - \eta \nabla_\theta \mathcal{L}(\theta)$

$n \leftarrow n + 1$

until convergence

Algorithm 6 Integration Flow Sampling Algorithm for PFGM++

Input: T , trained model parameter θ , sampling step $k, r_T = \sigma_T \sqrt{D}, R_T \sim p_{r_T}(R), \mathbf{v} = \frac{\mathbf{u}}{\|\mathbf{u}\|_2}$, with $\mathbf{u} \sim \mathcal{N}(\mathbf{0}, \mathbf{I})$,

initialize $\mathbf{x}_0^{(0)} \sim \mathcal{N}(\mathbf{0}, \mathbf{I})$

Compute $\mathbf{x}_T = R_T \mathbf{v}$

for $k = 0$ **to** $k - 1$ **do**

$\mathbf{x}_0^{(k+1)} \leftarrow g_\theta(\mathbf{x}_0^{(k)}, \mathbf{x}_T, T)$

end for

Output: $\mathbf{x}_0^{(n+1)}$

B. Proof of Theorems

B.1. Proof of Theorem 1:

Proof. Before proving the theorem, we prove the corollary first:

Corollary:

$$\mathbb{E} \left[(A - \mathbb{E}[A \mid B, C])^2 \right] \leq \mathbb{E} \left[(A - \mathbb{E}[A \mid B])^2 \right], \quad (44)$$

The variance of a random variable A can be decomposed as follows:

$$\text{Var}(A) = \mathbb{E}[\text{Var}(A \mid B)] + \text{Var}(\mathbb{E}[A \mid B]). \quad (45)$$

Now, introduce the extra information C . The variance of A , conditioned on both B and C , is:

$$\text{Var}(A \mid B, C) = \mathbb{E}[\text{Var}(A \mid B, C) \mid B] + \text{Var}(\mathbb{E}[A \mid B, C] \mid B) \quad (46)$$

Since conditioning on more information reduces uncertainty, we know that:

$$\text{Var}(A \mid B, C) \leq \text{Var}(A \mid B). \quad (47)$$

We also have:

$$\mathbb{E} \left[(A - \mathbb{E}[A \mid B, C])^2 \right] = \mathbb{E}[\text{Var}(A \mid B, C)] \quad (48)$$

and

$$\mathbb{E} \left[(A - \mathbb{E}[A|B])^2 \right] = \mathbb{E}[\text{Var}(A|B)] \quad (49)$$

Since $\text{Var}(A|B, C) \leq \text{Var}(A|B)$, it follows that:

$$\mathbb{E} \left[(A - \mathbb{E}[A|B, C])^2 \right] \leq \mathbb{E} \left[(A - \mathbb{E}[A|B])^2 \right] \quad (50)$$

let $\mathbf{x}_0 = A, \mathbf{x}_t = B, \mathbf{x}_0^{(n)} = C$, plug into the corollary, we complete the proof \square

B.2. Proof of Theorem 2:

Proof. The initial value problem (IVP) of the reversed time ODE can be expressed as:

$$\begin{cases} \frac{d\mathbf{x}_s}{ds} = v(\mathbf{x}_s, s) & s \in [0, t] \\ \mathbf{x}_t = \hat{\mathbf{x}}_t \end{cases} \quad (51)$$

if putting $\tilde{\mathbf{x}}_s := \mathbf{x}_{t-s}$, we get

$$\begin{cases} \frac{d\tilde{\mathbf{x}}_s}{ds} = -v(\tilde{\mathbf{x}}_s, s) & s \in [0, t] \\ \tilde{\mathbf{x}}_0 = \hat{\mathbf{x}}_t \end{cases} \quad (52)$$

The IVP 51 and 52 are equivalent and can be used interchangeably.

From the Lipschitz condition on v , we have:

$$\|v(\tilde{\mathbf{x}}_s, s) - v(\tilde{\mathbf{y}}_s, s)\|_2 \leq L \|\tilde{\mathbf{x}}_s - \tilde{\mathbf{y}}_s\|_2. \quad (53)$$

Use the integral form:

$$\|g(\mathbf{x}_0, \mathbf{x}_t, t) - g(\mathbf{y}_0, \mathbf{y}_t, t)\|_2 \leq \|\tilde{\mathbf{x}}_0 - \tilde{\mathbf{y}}_0\|_2 + \int_0^t L \|\tilde{\mathbf{x}}_s - \tilde{\mathbf{y}}_s\|_2 ds \quad (54)$$

By using Gröwnwall inequality, we have:

$$\|g(\mathbf{x}_0, \mathbf{x}_t, t) - g(\mathbf{y}_0, \mathbf{y}_t, t)\|_2 \leq e^{Lt} \|\tilde{\mathbf{x}}_0 - \tilde{\mathbf{y}}_0\|_2 = e^{Lt} \|\hat{\mathbf{x}}_t - \hat{\mathbf{y}}_t\|_2 \quad (55)$$

Next, consider the inverse time ODE, we have:

$$\|\mathbf{x}_t - \mathbf{y}_t\|_2 \leq \|g(\mathbf{x}_0, \mathbf{x}_t, t) - g(\mathbf{y}_0, \mathbf{y}_t, t)\|_2 + \int_0^t L \|\mathbf{x}_s - \mathbf{y}_s\|_2 ds \quad (56)$$

Again, by using Gröwnwall inequality,

$$\|\mathbf{x}_t - \mathbf{y}_t\|_2 \leq e^{Lt} \|g(\mathbf{x}_0, \mathbf{x}_t, t) - g(\mathbf{y}_0, \mathbf{y}_t, t)\|_2 \quad (57)$$

Therefore,

$$\|g(\mathbf{x}_0, \mathbf{x}_t, t) - g(\mathbf{y}_0, \mathbf{y}_t, t)\|_2 \geq e^{-Lt} \|\mathbf{x}_t - \mathbf{y}_t\|_2 \quad (58)$$

and we complete the proof of:

$$e^{-Lt} \|\mathbf{x}_t - \mathbf{y}_t\|_2 \leq \|g(\mathbf{x}_0, \mathbf{x}_t, t) - g(\mathbf{y}_0, \mathbf{y}_t, t)\|_2 \leq e^{Lt} \|\mathbf{x}_t - \mathbf{y}_t\|_2. \quad (59)$$

Since the neural network is sufficiently trained, we have:

$g_{\theta^*}(\mathbf{x}_0^{(n)}, \mathbf{x}_t, t) \equiv g(\mathbf{x}_0, \mathbf{x}_t, t)$, replace $g(\mathbf{x}_0, \mathbf{x}_t, t), g(\mathbf{y}_0, \mathbf{y}_t, t)$ with $g_{\theta^*}(\mathbf{x}_0^{(n)}, \mathbf{x}_t, t), g_{\theta^*}(\mathbf{y}_0^{(n)}, \mathbf{y}_t, t)$ respectively in (59), we obtain:

$$e^{-Lt} \|\mathbf{x}_t - \mathbf{y}_t\|_2 \leq \|g_{\theta^*}(\mathbf{x}_0^{(n)}, \mathbf{x}_t, t) - g_{\theta^*}(\mathbf{y}_0^{(n)}, \mathbf{y}_t, t)\|_2 \leq e^{Lt} \|\mathbf{x}_t - \mathbf{y}_t\|_2 \quad (60)$$

\square

B.3. Proof of Theorem 3:

Proof. For clarity within this particular theorem, we adopt the same notational convention as rectified flow: we label the initial (starting) points by \mathbf{x}_0 and the final (target) points by \mathbf{x}_1 . Everywhere else in the paper (outside this theorem), we follow the convention of diffusion model, where \mathbf{x}_0 denotes the sample to be recovered (the "target" in the diffusion context), and \mathbf{x}_1 or \mathbf{x}_T denotes the (noisy) starting sample.

$$\begin{aligned}
 & \min_v \int_0^1 \left\{ \int_{\mathbb{R}^D \times \mathbb{R}^D} \|(\mathbf{x}_1 - \mathbf{x}_0) - v(\mathbf{x}_t, t)\|^2 \pi(\mathbf{x}_0, \mathbf{x}_1) d\mathbf{x}_0 d\mathbf{x}_1 \right\} dt \quad // \text{Flow Matching objective} \\
 &= \min_v \int_0^1 E \left[\|(\mathbf{x}_1 - \mathbf{x}_0) - v(\mathbf{x}_t, t)\|^2 \right] dt \quad // \text{Rectified Flow objective} \\
 &= \min_v E \int_0^1 \|(\mathbf{x}_1 - \mathbf{x}_0) - v(\mathbf{x}_t, t)\|^2 dt \quad // \text{Fubini-Tonelli Theorem} \\
 &\geq \min_v E \left\| \int_0^1 (\mathbf{x}_1 - \mathbf{x}_0) - v(\mathbf{x}_t, t) dt \right\|^2 \quad // \text{Jensen's inequality} \\
 &= \min_v E \left\| \int_0^1 (\mathbf{x}_1 - \mathbf{x}_0) dt - \int_0^1 v(\mathbf{x}_t, t) dt \right\|^2 \\
 &= \min_G E \left\| \mathbf{x}_1 - \mathbf{x}_0 - \frac{G(\mathbf{x}_1, \mathbf{x}_t, t)}{t} \right\|^2 \quad // \text{Integration Flow by Equation (36),(37)}
 \end{aligned}$$

Therefore, Integration Flow models the transformation via a single integrated function G , which is sufficient and effectively optimal for solving the Flow-Matching/Rectified-Flow objective.

□